ANALYTICAL MODEL OF ELECTROMAGNETIC WAVES PROPAGATION AND LOCATION OF INCLINED PLASMA LAYERS USING OCCULTATION DATA

A. G. Pavelyev

Institute of Radio Engineering and Electronics of Russian Academy of Sciences (IRE RAS)
Fryazino, Vvedenskogo sq. 1, 141120 Moscow Region, Russia

Y. A. Liou

Center for Space and Remote Sensing Research
National Central University
Chung-Li 320, Taiwan

J. Wickert

Geo Forschungs Zentrum Potsdam (GFZ-Potsdam)
Telegrafenberg, Potsdam 14473, Germany

K. Zhang, C. S. Wang, and Y. Kuleshov

School of Mathemathical & Geospatial Sciences
RMIT University
GPO Box 2476V, Melbourne 3001, Australia

Abstract—An analytical model for the description of the electromagnetic waves propagation in a layered medium consisting of sectors having the locally spherical symmetric distributions of refractivity is introduced. Model presents analytical expressions for the phase path and refractive attenuation of electromagnetic waves. Influence of the inclined ionospheric layers is a cause of the ionospheric interference in the trans-ionospheric communication satellite-to-satellite or satellite-to-Earth links. It follows from the analytical model that the identification of the inclined ionospheric layers contributions and measurements of their location and parameters may be fulfilled by use of comparative analysis of the amplitude variations and the eikonal acceleration

of the RO signals. Model is applied to analysis of the radio occulta-
tion (RO) signals propagating through the ionosphere and atmosphere.
Model explains existence of the ionospheric contributions in the RO
signals at the altitudes 30–90 km of the RO ray perigee as connected
with influence of a tangent point in the ionosphere where the electron
density gradient is perpendicular to the RO ray trajectory. By use
of the CHAMP RO amplitude data a description of different types
of the ionospheric contributions to the RO signals is introduced and
compared with results of measurements obtained earlier in the commu-
nication link satellite-to-Earth at frequency 1.5415 GHz of MARSAT
satellite.

1. INTRODUCTION

The high-stability radio signals transmitted at two GPS frequencies
$f_1 = 1575.42$ MHz and $f_2 = 1227.60$ MHz from a GPS satellite and
received at a GPS receiver aboard a low earth orbit (LEO) small/micro
satellite are used for the radio occultation (RO) investigations [1–
6]. RO method is an effective tool for the investigation of the
Earth's atmosphere and ionosphere at different altitudes with a global
coverage [7, 8]. When applied to ionospheric investigations RO method
may be considered as a global tool and can be compared with the
global earth- and space-based radio tomography [9, 10]. However,
the horizontal gradients in the ionosphere may introduce significant
interference in the RO investigations of the ionosphere and atmosphere.
The mechanism of the ionospheric interference may be revealed by
use of an analytical model considering the propagation medium as
consisting of locally spherical symmetric sectors.

During a RO event the radio ray linking a LEO GPS receiver
to a GPS satellite transmitter (marked by points L and G in Fig. 1,
respectively) immerses gradually into the ionosphere and atmosphere.
The LEO receiver measures the GPS dual-frequency phase delays and
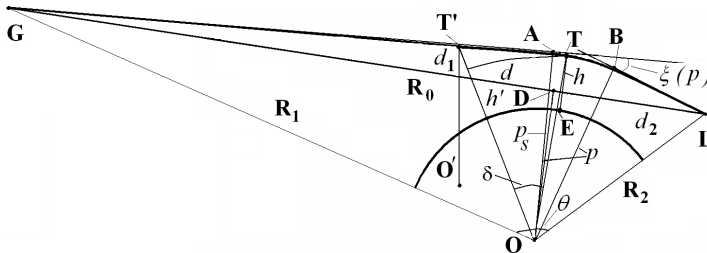

Figure 1. Geometry of radio ray path in RO experiment.

amplitudes of RO signal for subsequent retrieval of the vertical profiles of the physical parameters of the ionosphere and atmosphere. In the case of absence of multipath propagation the RO inversion technique is based on two implicit assumptions: (i) the tangent point T, where the refractivity gradient is perpendicular to the RO ray direction, coincides with the RO ray perigee (Fig. 1), and (ii) the tangent point T is only one on the RO ray trajectory GTL. Under these assumptions, despite a prolonged path GTL, a relatively small area with center at point T introduces the main contribution to the amplitude and phase variations of the RO signals [11]. In this case the amplitude and phase variations of the RO signals are functions of the ray perigee height $H(T)$ (Fig. 1) and the satellites' positions and velocities. These functions can be used to determine the height dependence of the bending angle $\xi(p(H))$ if precise orbital data are given [1, 2, 12]. Then Abel transform is applied to obtain the vertical profiles of the electron density in the ionosphere and refractivity in the atmosphere as functions of the ray perigee height H [6, 13–16]. Amplitude data can also be used to obtain the vertical gradients of the electron density in the ionosphere and refractivity in the atmosphere independently [17, 18].

RO measurements in the atmosphere can be impacted by ionospheric contributions because RO signal propagates through two different parts of the ionosphere. Usually the ionospheric influence may be described as a relatively slow change in the phase path excess without noticeable variations in the amplitude of RO signal. This change can be excluded by different methods of ionospheric correction [1, 19].

Physical changes in the near-Earth space environment in response to variations in solar radiation, solar plasma ejection, and the electromagnetic status of the interplanetary medium produce disturbances in the ionosphere. Disturbed ionosphere significantly changes not only the phase but also the amplitude of the RO signals. Phenomenon of strong amplitude and phase frequency dependent variations in RO signals is often observed within the altitudes of $H(T)$ between 40 and 90 km above the main part of the neutral atmosphere and below the E-layer of the ionosphere. This effect is a subject for analysis in this paper.

The goal of this paper is (i) to introduce the description of different kinds of the ionospheric influence on the RO signals within the altitudes of $H(T)$ between 40 and 90 km, (ii) to present an analytical model for the refractive attenuation and phase path excess of electromagnetic waves in locally spherical symmetric media, and (iii) to demonstrate the possibility to identify contributions and to measure parameters of the inclined plasma layers by means of analyzing CHAMP RO

experimental data. The paper is structured as follows. In Section 2, the description of different kinds of the ionospheric influence on CHAMP RO signal is presented. Section 3 introduces an analytical model of wave propagation through the ionosphere and atmosphere of the Earth. In Section 4, an example of ionospheric layers identification and the electron density retrieval is considered. Conclusions are given in Section 5.

2. TYPES OF IONOSPHERIC INFLUENCE ON CHAMP RO SIGNAL

The radio occultation experiment aboard CHAMP was activated on February 11, 2001 [6]. Occultation measurements of the ionosphere and neutral atmosphere are scheduled autonomously by the BlackJack receiver instrument. Carrier phase at two frequencies f_1, f_2, and signal-to-noise ratio (SNR) at frequency f_1 are recorded at a sampling rate of 50 Hz. Previously, the RO technology has been based mainly on analyzing the phase of the electromagnetic wave after propagating through the ionosphere and atmosphere [2]. The amplitude of RO signal presents new potential and capability for the research and simultaneous observations of the atmosphere and ionosphere [11, 15, 17, 18, 20–24]. High sensitivity of the amplitude variations to ionospheric plasma layers can be used for description of different kinds of the ionospheric influence on RO signals in the trans-ionospheric communication links. In the case of CHAMP RO experiments quiet ionospheric conditions have come to light in the form of small values of the S_4 index of the amplitude scintillations averaged at the altitudes H in the 40–90 km interval:

$$S_4 = [< (I(t) - < I >)^2 > / < I >^2]^{1/2} \qquad (1)$$

where I is the intensity of the RO signals and $< I >$ is the average intensity of the RO signals corresponding to the propagation in the open space. An example of quiet ionospheric conditions observed during the CHAMP RO experiments is shown in Fig. 2 (left panel). The amplitude curve has low variations with index $S_4 = 0.06$. The phase path excesses $\Phi_1(t)$ and $\Phi_2(t)$ at frequencies f_1, and f_2 are shown by curves F_1 and F_2. The curves F_1 and F_2 have been obtained after subtracting a regular phase trend connected with influence of the upper ionosphere. The curve F0 relates to combined phase $\Phi(t)$, obtained from the ionospheric correction formula [1]:

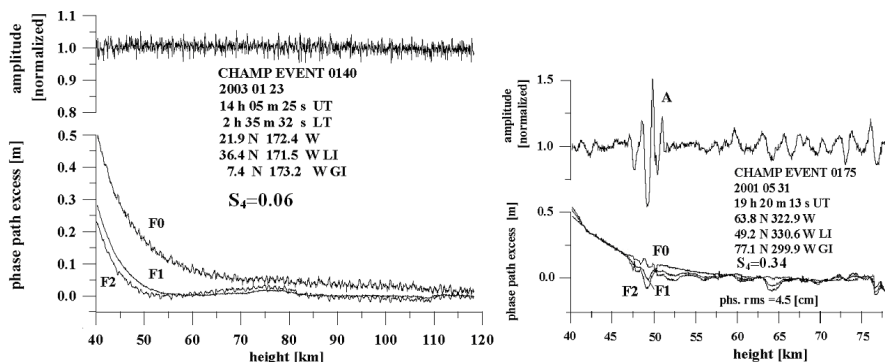$$\Phi(t) = [f_1^2 \Phi_1(t) - f_2^2 \Phi_2(t)]/(f_1^2 - f_2^2) \qquad (2)$$

Figure 2. Amplitude and phase measurements of the CHAMP RO signals in the case of quiet (left) and disturbed (right) ionosphere (events No. 0140 and 0175, January, 23, 2003). The insert indicates the time of the event, coordinates of the atmospheric tangent point T, coordinates of the intersection of the ionosphere at the height of 280 km from the site of LEO satellite (letters "LI") and GPS satellite (letters "GI"). The S_4 index value is shown in the lower line of the insert.

Examples of significant variations of the phase and amplitude of the GPS RO signals are given below in the altitude intervals of the ray perigee 40–90 km. These examples support suggestion that there exist the inclined ionospheric layers located along the RO ray trajectory. According to Fig. 1, the apparent displacement of the height of the ionospheric layer Δh can be used for estimating its inclination δ with respect to the local horizontal direction [23]:

$$\delta \approx (2\Delta h/a)^{1/2} \tag{3}$$

where a is the Earth's radius (Fig. 1). One can estimate using Fig. 1 the horizontal distance d between the atmospheric and ionospheric tangent points if Δh is known as $d \approx (2\Delta ha)^{1/2}$. The isolated quasi-regular event with the influence of the sporadic E-layer is shown in Fig. 2 (right panel). The fine structures corresponding to an inclined sporadic E-layer are seen in the height $H(T)$ intervals of 45–50 km. The phase and amplitude vertical distributions can correspond to the inclined sporadic E-layers usually located at the height about 93–103 km in the evening ionosphere. One can estimate the displacement of the ionospheric tangent point from (2). For $\Delta h \approx 50$ km, one can obtain $\delta \approx 6°$ and $d \approx 700$ km again from (2). These values may correspond to the sporadic E-layer at the height of 98 km declined by $6°$ relative to horizon and located at the distance of 700 km away from

the atmospheric tangent point in the RO plane.

An example of event with high quasi-regular variations in the amplitude and phase of RO signal with magnitude of index $S_4 = 0.34$ is shown in Fig. 3(a). The phase paths at two frequencies are highly correlated and change in the interval $-0.3 \leq \Phi_{1,2} \leq 0.5\,\text{m}$. These variations may be connected with waves in the electron density distribution. Strong ionospheric influence with diffraction structures in the RO signals is demonstrated in Fig. 3(b). The diffraction pattern is seen at the heights between $H(T) = 60\,\text{km}$ and $H(T) = 62.5\,\text{km}$. This case can be considered as a consequence of diffraction of electromagnetic waves on sharp gradients of the electron density in an inclined sporadic E-layer. Example of a noisy CHAMP event with high amplitude variations ($S_4 = 0.26$) is shown in Fig. 3(c). This event can be classified as a typical case, relevant to a noisy ionospheric contribution caused by intense ionospheric irregularities in the equatorial region in the midnight at $02\,\text{h}$ Local Time (LT). The main part of the amplitude variations is limited to the interval $0.7 \leq A \leq 1.2$. The phase variations are also high indicating sharp changes in the TEC that may possibly correspond to bubbles moving in the disturbed region of the ionosphere.

According to the analysis of CHAMP RO amplitude and phase data, five types of ionospheric influence on the RO signals can be established at the altitudes of $40\,\text{km}$–$90\,\text{km}$:
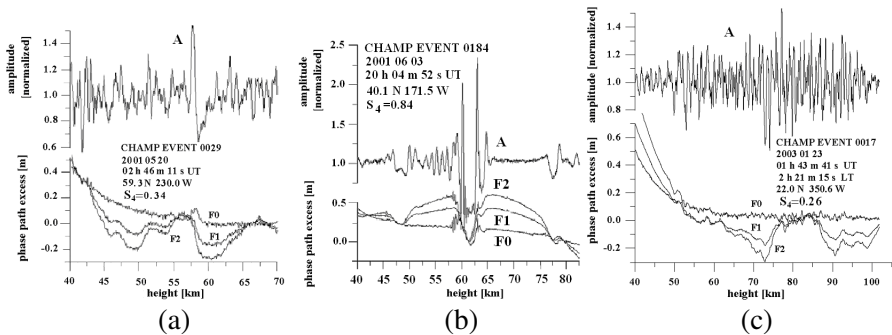

Figure 3. (a) Quasi-regular variations in the amplitude and phase values of the CHAMP RO signals for event No. 0029 (May 20, 2001). (b) Amplitude and phase values of the CHAMP RO signal owing to diffraction of electromagnetic waves in the ionosphere (event No. 0184, June 03, 2001. (c) Amplitude and phase values of the CHAMP RO signal for noisy event (No. 0017, January 23, 2001) with high amplitude variations ($S_4 = 0.26$) near geomagnetic equator at local night.

- Quiet events (type 1, Fig. 2, left).
- Isolated quasi-regular flashes in the amplitude and phase of RO signal (type 2, Fig. 2, right).
- Regular events with quasi-periodical contributions to the amplitude of RO signal (type 3, Fig. 3(a)).
- Diffractive events with diffraction phenomena in the ionosphere (type 4, Fig. 3(b))
- Noisy events with highly incoherent contribution of the iono-spheric disturbance to the amplitude of RO signal (type 5, Fig. 3(c)).

These types can be compared with the results obtained earlier. The temporal characteristics of the signals from a MARISAT satellite over the Indian Ocean at an elevation angle of 17.3 deg using a long term (16 months) measurements were investigated [25]. Both C- and S-types of the ionospheric amplitude scintillations of radio signals are identified. The C-type is similar to noisy variations without any significant regular or periodical structure in the amplitude changes of the trans-ionospheric signals. The S-type consists of quasi-regular structures which can be associated with the influence of the bubbles or other types of disturbances in the ionospheric plasma [23]. The CHAMP RO amplitude variations can be recognized also as the C- and S-types of amplitude scintillations classified previously in the communication INMARSAT link at the same frequency band near 1.5 GHz.
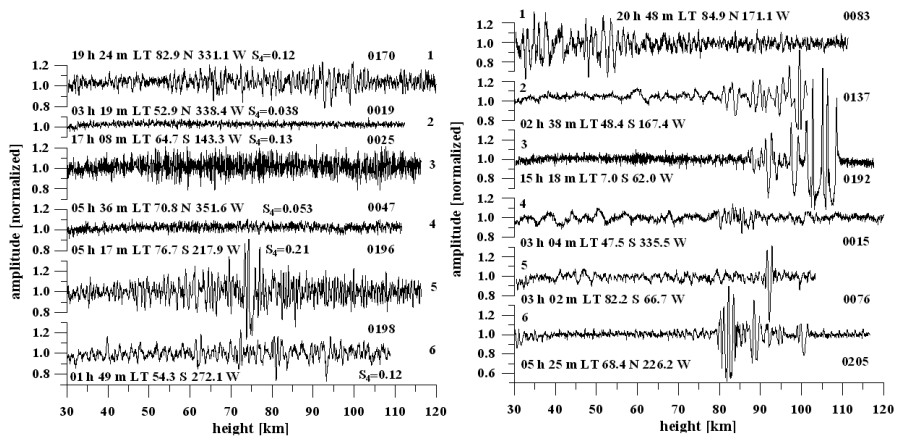

Figure 4. C-type noisy (left) and S-type quasi-regular (right) amplitude scintillations of the CHAMP RO signal. The legends indicate the local time (LT), the geographical coordinates, magnitude of the S_4 index, and event's number of the RO experiments.

The noisy C-type amplitude variations in the CHAMP RO signals at the altitudes of $30\,\text{km}$–$120\,\text{km}$ are shown in Fig. 4 (left panel). Curves $1, 3$–5 describe scintillations observed in the North and South Polar regions during the RO events of No. 0170, No. 0025, No. 0047, and No. 0196 (on January 23, 2003). For events No. 0170, No. 0025, and No. 0196 S_4 index was equal to 0.12, 0.13, 0.21 (curves 1, 3, and 5, respectively), that corresponds to disturbed ionospheric conditions. Event No. 0047 corresponds to the weakly disturbed ionosphere with S_4 index equal to 0.053. Curves 2 and 6 (RO events No. 0019 and No. 0198, January 23, 2003) are relevant to the mid-latitudes with quiet (curve 2, $S_4 = 0.038$) and disturbed (curve 6, $S_4 = 0.12$) ionosphere. The amplitude fluctuations during the RO event No. 0019 in the height interval of $H(T) = 30$–$110\,\text{km}$ (curve 2) were caused mainly by random receiver noises. The geographical position and local time of the noisy RO events correspond to the same parameters of the noisy amplitude scintillations observed previously in trans-ionospheric communications [25, 26].

Quasi-regular S-type amplitude variations are shown in Fig. 4, right panel. Curves 2 and 4 correspond to the CHAMP RO events No. 0137 and No. 0015 (January 23, mid-latitude nighttime ionosphere) respectively; curves 1, 3, and 5 relate to events 0083, 0192, and 0076; and curve 6 corresponds to event No. 0205, January 23, 2003 (equatorial daytime, south and north polar ionosphere). Inclined plasma layers in the E- or F-regions of the ionosphere might be a cause of the quasi-regular amplitude variations.

Through comparisons of the data shown in Fig. 2–Fig. 4, the types 2, 3 and 4 of RO amplitude variations can be recognized as S-type amplitude scintillations observed in the trans-ionospheric INMARSAt link [23]. The noisy variations in the CHAMP RO signals correspond to the amplitude scintillations of C-type. This coincidence in the types of CHAMP RO amplitude scintillations and the amplitude variations observed in the Earth-based experiments indicates common ionospheric mechanisms of their origin.

3. ANALYTICAL MODEL FOR THE PHASE PATH EXCESS AND REFRACTIVE ATTENUATION OF RO SIGNALS

One can assume a locally spherical symmetry of the electron density distributions along the ray trajectory in the entrance and exit parts of the ionosphere. These parts of the ionosphere may have different centers of spherical symmetry (e.g., point O' in Fig. 1). The amplitude and phase variations of RO signals in this case may be investigated

using analytical models. The analysis of RO signal variations can then be used to find the distribution of the electron density and to estimate the location of the inclined layers in the ionosphere according to method described [27, 28].

A medium model composed of several spherical sectors was applied previously to estimate the effects of horizontal gradients in the atmosphere [28]. A new analytical model describing changes of the phase path and refractive attenuation of electromagnetic waves propagated in the ionosphere and atmosphere is introduced. Three centers of locally spherical symmetry associated with a single RO ray path in the ionosphere and atmosphere are located at different points O_1, O_2, and O_3 corresponding to three parts of the ray trajectory $G_1B_1B_2L$ in three spherical sectors having boundaries at points B_1 and B_2, respectively: G_1B_1 (the ionosphere between transmitter G_1 and atmosphere), B_1B_2 (atmospheric part), and B_2L (the ionosphere between the receiver and atmosphere) (Fig. 5). Points G_1, L, O_1, O_2, and O_3 are assumed to belong to the plane $G_1B_1B_2L$. This assumption corresponds to experimental RO data indicating a significant refraction effect in the plane of propagation. The central angles θ_1, θ_2, and
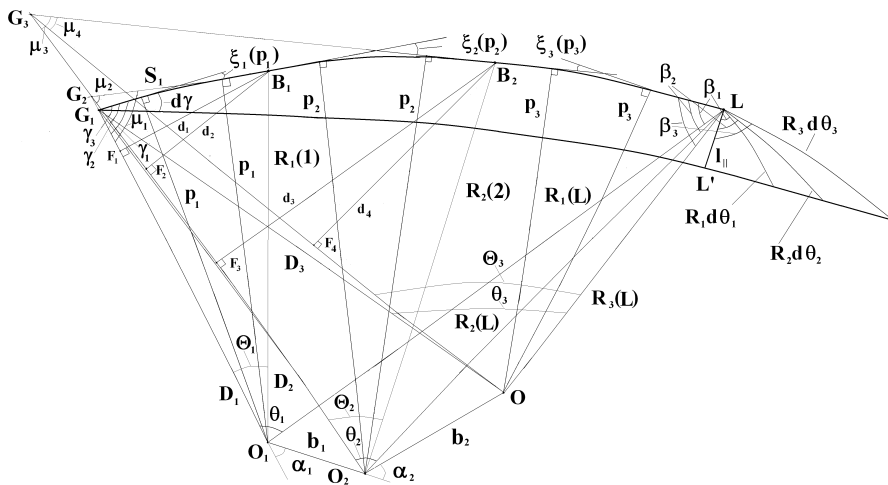

Figure 5. Section of the ray tube by RO plane containing transmitter G_1, receiver L and centers of locally spherical symmetry O_1, O_2, and O_3. Lines G_1L and G_1L' are the top and bottom boundaries of the ray tube, respectively. Points B_1 and B_2 are the boundaries between two parts of the ionosphere G_1B_1 and B_2L, and atmosphere B_1B_2, angles ξ_1, ξ_2 and ξ_3 are the bending angles corresponding to the three parts of RO ray G_1B_1, B_1B_2, and B_2L.

θ_3 between directions to transmitter G_1 and receiver L have vertices located at points O_1, O_2, and O_3 (Fig. 5). The distances G_1O_1, G_1O_2, and G_1O_3 and LO_1, LO_2, and LO_3 are equal to D_1, D_2, and D_3, and $R_1(L)$, $R_2(L)$, and $R_3(L)$, respectively. Lines G_1L and G_1L' are, accordingly, the sections of the top and bottom boundaries of a ray tube by the RO plane. Points G_2 and G_3 (actually G_2 and G_3 are apparent radio images of transmitter G_1 as seen from points B_1 and B_2) are intersections of the tangents to the RO ray trajectory $G_1B_1B_2L$ at the points B_1 and B_2 with the straight lines O_1G_1 and O_2G_2, respectively. The angles μ_1, μ_2 and μ_3, μ_4 have common vertices at the points G_2 and G_3. Variables μ_1, μ_2 are the angles between the tangent to the ray trajectory $G_1B_1B_2L$ at point B_1 and directions of O_1G_2 and O_2G_2, respectively, (Fig. 5). Variables μ_3, μ_4 are the angles between the straight line G_3B_2 — the tangent to the ray trajectory $G_1B_1B_2L$ at point B_2 and directions of O_2G_3 and O_3G_3, accordingly, (Fig. 5). Dependence of the phase path excess and refractive attenuation on the impact parameter p may be considered separately for three parts of RO ray trajectory $G_1B_1B_2L$. The phase path Φ corresponding to the ray $G_1B_1B_2L$ (Fig. 5) is a sum:

$$
\begin{aligned}
&\Phi = \sum_{i=1}^{i=N} \Phi_i; \quad \Phi_i = L_i(p_i) + \kappa_i(p_i) \\
&L_i(p_i) = \sqrt{R_i^2(i-1) - p_i^2} \pm \sqrt{R_i^2(i) - p_i^2} + p_i\xi_i(p_i), \\
&\xi_i(p_i) = -d\kappa_i(p_i)/dp_i
\end{aligned}
\tag{4}
$$

where N is a number of spherical sectors influencing on the trajectory $G_1B_1B_2L$, $N = 3$ for the geometry shown in Fig. 5; $R_i(l-1)$ and $R_i(l)$ are the distances from the i-th spherical sector center O_i to the input and output of the l-th spherical sector coinciding with boundaries B_{i-1}, B_i; for the case $N = 3B_0$ and B_3 coincide with G_1 and L, respectively, B_1 and B_2 are shown in Fig. 5; $R_1(0) = D_1$; $p_i, \xi_i(p_i), \kappa_i(p_i)$ are the impact parameter, the bending angle and the main refractivity part of the phase path corresponding to the i-th spherical sector; $L_i(p_i)$ is the geometrical part of the phase path inside the i-th spherical sector, the sign "+" should be chosen when the tangent point is located on the ray trajectory G_1L inside the i-th spherical sector, and the sign "-" should be chosen in the opposite case. The refractive index at the boundaries B_{i-1}, B_i, $i = 2, \ldots, N$ is assumed to be equal 1. The distances $R_i(l-1)$ and $R_i(l)$ may be determined using the impact parameters p_i, $i = 1, \ldots, N$, if the angular coordinates of boundaries B_{i-1}, B_i defined by the angles $\Theta_1, \Theta_2, \Theta_3$ (Fig. 5) are known. Equation (4) for the phase path Φ is valid for the general case when the number N of

spherical sectors is arbitrary under the assumption that all centers of spherical symmetry belong to the occultation plane.

A method applied previously to the case of a spherically symmetric medium is used below in the geometric optics approximation to obtain an exact expression for the refractive attenuation of electromagnetic waves X_L [29]. We choose a ray tube bounded by four surfaces, two of them (G_1FLC and $G_1AL'D$) are perpendicular to the plane $G_1B_1B_2L$ and intersect this plane along the rays G_1L and G_1L', respectively, (Fig. 6). This ray tube has nearly rectangular cross section AFCD at the point L with the sizes $l_\parallel$ and $l_\perp$ in the plane surface $G_1B_1B_2L$ and in the perpendicular plane, correspondingly, (Fig. 5 and Fig. 6). Owing to the locally spherical symmetry the tangents to the rays
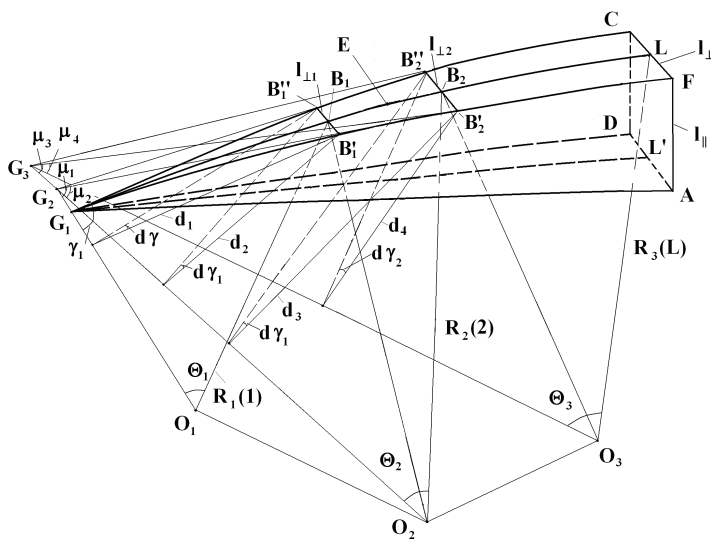

Figure 6. Geometry of a ray tube of electromagnetic waves propagating through three spherical symmetric sectors. Points G_1, B_1, B_2, L are supposed to be located in the same plane with the centers of spherical symmetry O_1, O_2, and O_3. Points G_2 and G_3 are intersections of the tangents to the ray trajectory $G_1B_1B_2L$ at the points B_1 and B_2 with the straight lines O_1G_1 and O_2G_2, respectively. The angles Θ_1, Θ_2, and Θ_3 have vertices at points O_1, O_2, and O_3. The values Θ_1, Θ_2, and Θ_3 determine the angles between directions O_1G1, O_2G_2, O_3G_3, and O_1B_1, O_2B_2, O_3L, correspondingly. The exit ray tube cross section AFCD at point L is nearly rectangular and have the sizes $l_\parallel$ and $l_\perp$ in the plane surface $G_1B_1B_2L$ and in the perpendicular plane, respectively.

G_1F, G_1L, and G_1C at the points B_1', B_1, and B_1'' intersect the straight line O_1G_1 at the point G_2 located in the plane $G_1B_1B_2L$ (Fig. 6). Therefore G_2 is a radio image of transmitter G_1 as seen from the boundary of the first and second sectors — point B_1. The plane $O_1G_1B_1B_2L$ is bisection of the surfaces O_1G_1AF and O_1G_1CD. Symmetry of the surfaces O_1G_1AF and O_1G_1CD allows one to find independent analytical expressions for the sizes $l_\parallel$ and $l_\perp$. We consider the distance $l_\perp$ between two symmetrical rays G_1F and G_1C located in the opposite side walls G_1AF and G_1CD (Fig. 6). The surfaces $O_1G_1B_1'$ and $O_1G_1B_1''$ form two plane side walls of the ray tube in the first spherical sector. The planes $O_1G_1B_1'$ and $O_1G_1B_1''$ intersect along the straight line G_1O_1 forming the dihedral angle $d\gamma$ (Fig. 6). The angle between the rays G_1L and G_1L' in the RO plane $G_1B_1B_2LL'$ at the point G_1 is also assumed to be equal $d\gamma$. In the second spherical sector these rays propagate according to the locally spherical symmetry in the planes containing the center O_2 and the rays' tangents at the points B_1' and B_1''. These planes are intersecting along the straight line O_2G_2 (Fig. 5 and Fig. 6) and form the dihedral angle $d\gamma_1$. The distance $l_{\perp 1}$ at the boundary B_1 of the first spherical sector between the rays G_1B_1' and G_1B_1'' (Fig. 5 and Fig. 6) is described by next equations:

$$l_{\perp 1} = d_1 d\gamma; \quad d_1 = S_1 \sin \mu_1 \tag{5}$$

where S_1 is the distance G_2B_1 (Fig. 5). At the boundary B_1 in the second spherical sector the distance $l_{\perp 2}$ between the rays $B_1'B_2'$ and $B_1'B_{12}''$ is equal to:

$$l_{\perp 2} = d\gamma_1 d_2; \quad d_2 = S_1 \sin \mu_2 \tag{6}$$

where d_1, d_2 are the lengths of the perpendiculars from the point B_1 on the straight lines O_1G_2 and O_2G_2, correspondingly, (Fig. 5). The size $l_\perp$ satisfies a continuity requirement at the first two sector's boundary B_1.

$$l_{\perp 1} = l_{\perp 2} \tag{7}$$

A connection between the dihedral angles $d\gamma$ and $d\gamma_1$ follows from Equations (5)–(7):

$$\begin{aligned} d\gamma_1 &= d\gamma d_1/d_2, \quad d_1/d_2 = \sin \mu_1 / \sin \mu_2, \\ d\gamma_1 &= d\gamma \sin \mu_1 / \sin \mu_2 \end{aligned} \tag{8}$$

From (6) and (8), the distance $l\perp_2$ in the second sector can be expressed as:

$$l_{\perp 2} = d\gamma_1 d_2(E) = d\gamma d_2(E) \sin \mu_1 / \sin \mu_2, \tag{9}$$

where $d_2(E)$ is the length of the perpendicular from the current point E on the straight line O_2G_2. The same procedure can be applied to

find the dihedral angle $d\gamma_2$ at the boundary B_2 between the second and the third sectors:

$$d\gamma_2 = d\gamma_1 d_3/d_4, \quad d_3/d_4 = \sin \mu_3/\sin \mu_4,$$
$$d\gamma_2 = d\gamma_1 \sin \mu_3/\sin \mu_4 = d\gamma \sin \mu_1 \sin \mu_3/(\sin \mu_2 \sin \mu_4) \tag{10}$$

The length $l_{\perp 3}$ of the ray tube at point L can be found from the following equation:

$$l_{\perp 3} = d\gamma d_4(L) \sin \mu_1 \sin \mu_3/(\sin \mu_2 \sin \mu_4) \tag{11}$$

where $d_4(L)$ is the length of the perpendicular from point L on the line O_3G_3 (Fig. 6). Owing to the locally spherical symmetry the tangents to the rays G_1F, G_1L, and G_1C at points B_2', B_2, and B_2'' intersect the straight line O_1G_1 in the point G_3 located in the plane $G_1B_1B_2L$ (Fig. 6); μ_3, μ_4 are the angles with a common vertex at the point G_3 between the tangent to the ray GF at the point B_2' and directions O_2G_3 and O_3G_3, respectively, (Fig. 6). From Equations (6)–(11) the size $l_{\perp 3}$ then depends on locations of the boundaries B_1, B_2 and centers of spherical sectors O_1, O_2, O_3.

The size $l_{\parallel}$ at point L may be found independent of the size $l_{\perp}$ by considering the rays G_1L and GL' in the plane $G_1LO_1O_2O_3$, which is the vertical section of the ray tube (Fig. 5). The central angles $\theta_1, \theta_2, \theta_3$ between the directions to the transmitter G_1 and receiver L have vertices in the centers O_1, O_2, and O_3 of spherical sectors. The impact parameters in the corresponding spherical sectors are designated by p_1, p_2, and p_3 (Fig. 5). Owing to the condition of spherical symmetry the impact parameters p_1, p_2, and p_3 satisfy to the following relationships which are valid inside the i-th spherical sector:

$$p_i = n(R_i)R_i \sin \gamma_e, \ i = 1, 2, 3 \tag{12}$$

where $n(R_i)$ is the refractive index, γ_e is the angle between the tangent to the ray trajectory G_1L at the current point E and direction to the center of spherical sector. The tangents to the ray trajectory G_1L and the directions to the centers O_1, O_2, and O_3 make the angles γ_1, γ_2 , and γ_3 at the point G_1 and β_1, β_2, and β_3 at the point L, respectively (Fig. 5). A method applied previously for the case of a spherically symmetric medium [29] may be used to obtain an exact expression for the size $l_{\parallel}$. Three expressions are following under taking into consideration the rectangular triangles having the common cathetus LL' ($l_{\parallel}$), and the differentials $R_i d\theta_i$ as the hypotenuses (Fig. 5):

$$l_{\parallel} = R_i(L) cos\beta_i \partial\theta_i/\partial\gamma_1 d\gamma, \ i = 1, 2, 3 \tag{13}$$

where $R_i(L)$ are the distances O_iL, $i = 1, 2, 3$ (Fig. 5). Note that the partial derivatives of the central angles θ_i relative to the input angle γ_1 are evaluated with the distances $R_1(L), R_2(L), R_3(L)$ and

$D_1(G_1), D_2(G_1), D_3(G_1)$ are held constant. The relationship (13) is valid for an arbitrary number i from the interval $i = 1, 2, 3$. The power W emitted by an isotropic antenna in the ray tube is equal to:

$$W = Pd\Omega/4\pi = P\sin\gamma_1(d\gamma)^2/4\pi, \tag{14}$$

where P is the power of the transmitter, $d\Omega$ is the solid angle relevant to the ray tube.

The power flow in free space W_{L0} is equal to:

$$W_{L0} = P/4\pi R_0^2 \tag{15}$$

The refractive attenuation of electromagnetic waves at the point L X_L can be obtained as a ratio of the power flow in the ray tube $W_L = W/(l_\perp \cdot l_\parallel)$ to the power flow in free space W_{L0} (15):

$$
\begin{aligned}
&X_L = W_L/W_{L0} = R_0^2 sin\gamma_1/ \\
&[d_4(L)R_i(L)cos\beta_i\,|\partial\theta_i/\,\partial\gamma_1|\sin\mu_1\sin\mu_3/(\sin\mu_2\sin\mu_4)], \\
&i = 1, 2, 3; \quad d_4(L) = R_3(L)\sin[\Theta_3(L)]
\end{aligned} \tag{16}
$$

where $\Theta_3(L)$ is the angle with vertex at point O_3 between directions O_3G_3 and O_3L (Fig. 5 and Fig. 6). Relationships between the impact parameters p_1, p_2, p_3 central angles θ_1, θ_2, and θ_3 and bending angles ξ_1, ξ_2, and ξ_3 can be obtained using the geometry of the ray path $G_1B_1B_2L$ shown in Fig. 5:

$$p_2 = p_1 + b_1\sin(\gamma_1 - \xi_1 - \alpha_1); \ p_3v = p_2 + b_2\sin(\gamma_2 - \xi_1 - \xi_2 - \alpha_2) \tag{17}$$

$$\theta_i = \pi + \xi(p_1) - \gamma_i - \beta_i, \ \xi(p_1) = \xi_1(p_1) + \xi_2(p_2) + \xi_3(p_3); \ i = 1, 2, 3 \tag{18}$$

Relationships (4), (16)–(18) present main content of the analytical model in the partial case of three spherical sectors. In the plane of the electromagnetic waves propagation $G_1B_1B_2L$ the phase path and the refractive attenuation depend, respectively, on the sum of the phase changes and the bending angles in the spherical sectors and practically do not depend on the location of their boundaries. The refraction in the cross direction does not influence significantly on the phase path and the refractive attenuation. The effects of a spherically symmetric layer do not depend significantly on its location in the first, second or third spherical sectors. Any intense locally spherical symmetric layer along the ray $G_1B_1B_2L$ in the ionosphere may produce the unexpected strong variations in the amplitude and phase of the RO signals at the 40–90 km altitudes of the RO ray perigee because of values of the impact parameters in an inclined ionospheric and atmospheric layer are different. Therefore displacement of the tangent point is a main cause of systematic error in RO estimation of the altitude of inclined ionospheric layers. This conclusion may be valid also in

the case of electromagnetic waves propagation in the satellite-to-Earth communication links.

The introduced model may be generalized for an arbitrary number N (i.e., the number of spherically symmetric sectors with centers of spherical symmetry located in the same plane). For description of this case one can use the equations $(4),(11),(13),(16)$–(18). For the refractive attenuation in general case of N spherical sectors with coplanar centers one can obtain:

$$l_{\perp N}=d\gamma d_{2N-2}(L)S(1)\ldots S(N-1), \ \ S(i)=\sin\mu_{2i-1}/\sin\mu_{2i},$$
$$S(0)=1 \tag{19}$$
$$l_{\parallel} = R_i(L)\cos\beta_i\partial\theta_i/\partial\gamma_1 d\gamma \tag{20}$$
$$X_L = R_0^2\sin\gamma_1/\{R_i\cos\beta_i\,|\partial\theta_i\,/\,\partial\gamma_1|\,d_{2N-2}(L)S(1)\ldots S(N)\},$$
$$i=1,\ldots,N;\quad d_{2N-2}(L)=R_N(L)\sin[\Theta_N(L)] \tag{21}$$
$$\theta_i(L)=\pi+\xi\,(p_1)-\gamma_i-\beta_i,\ i=1,\ldots,N \tag{22}$$
$$\xi(p_1)=\xi_1(p_1)+\cdots+\xi_N(p_N) \tag{23}$$
$$p_i=p_{i-1}+b_{i-1}\sin(\gamma_{i-1}-\xi_1-\cdots-\xi_{i-1}-\alpha_{i-1}),\ i=2,\ldots,N \tag{24}$$

The subscripts in (19)–(24) denote a number of spherical sectors, the integer arguments correspond to a number of a boundary; $d_{2N-2}(L)$ is the length of the perpendicular from point L on the straight line connecting the center of the N-th spherical sector — point O_N with point G_N. The angles μ_{2k-1},μ_{2k} have common vertex at point G_k, $\mu_{2k-1},\,\mu_{2k}$ are the angles between the ray tangent $G_k B_{k-1}$ and the straight lines $G_k O_{k-1}, O_k G_k$, respectively. Relationship (21) for the refractive attenuation X_L is valid for any arbitrary number i from the interval $i=1,\ldots,N$.

The developed analytical model allows ray tracing of the RO signals. If the impact parameter p_1 is known then one can consequently determine the impact parameters p_i, $i=2,\ldots,N$ from Equation (24) and the refraction angle $\xi(p_1)$ and then recalculate the phase path $\Phi(p_1)$ and the refractive attenuation X_L from (16) for $N=3$ or from (21) for arbitrary N. It is necessary to note the important feature of the introduced model. If in the k-th sector the refraction effect is absent, then the dimension N of model can be lowered to $N-1$. In this case the next equality fulfills:

$$\mu_{2k-1}=\mu_{2k};\quad S(k)=1 \tag{25}$$

and the refractive attenuation (21) does not depend on the contribution from the k-th spherical sector.

The phase path of electromagnetic waves after propagating through the ionosphere and atmosphere may be considered according to relationship (4) as a linear function of the refraction angles in the

corresponding sectors. Therefore the linear methods of ionospheric correction introduced earlier [1, 19] should be effective in the case of propagation through several spherically symmetric sectors in the case of undisturbed ionosphere. However, the amplitude of RO signal is a nonlinear function of the refraction angle and in the case of the disturbed ionosphere it is a subject for strong perturbations.

Let us consider the partial cases. In the first case the refraction effect exists in the first sector according to the ionospheric influence and is absent in the remaining $N - 1$ sectors. This case is typical for the amplitude and phase variations at the altitudes 40–90 km where the neutral atmosphere's influence is minimal. In this case the points $G_2, G_3, \ldots, G_N$ are coinciding. As a consequence, the next relationship is fulfilled:

$$\mu_3 = \mu_2, \quad \mu_5 = \mu_4, \quad \ldots, \quad \mu_{2N-3} = \mu_{2N-4} \tag{26}$$

After substitution of Equation (26) in the relationship (21) one can obtain:

$$X_L = R_0^2 \sin \gamma_1 / [R_1^2(L) \cos \beta_1 |\partial \theta_1 / \partial \gamma_1| \sin \theta_1(L)] \tag{27}$$

Equation (27) has been obtained previously [29]. If the tangent point exists in the first sector, and there is a sharp gradient of refractivity, then one can observe in this case strong variations of the amplitude and phase of the RO signals at the low altitudes of RO rays perigee H 40 km–90 km because of a significant displacement of the centre of the first sector O_1. However, according to spherical symmetry one may estimate the electron density distribution in inclined ionospheric plasma layers by using the Abel transformation.

The case corresponding to refraction effect in two spherical sectors can be considered separately (Fig. 7). For this case one can obtain for the refractive attenuation the following relationship:

$$\mu_1 = \gamma_1 - \xi_1, \ \mu_2 = \mu_1 - \tan^{-1}[b_1 \sin \alpha_1 \sin \mu_1 / (b_1 \sin \alpha_1 \cos \mu_1 + p_2)]$$
$$X_L = R_0^2 \sin \gamma_1 / \{R_i(L) \cos \beta_i |\partial \theta_i / \partial \gamma_1| R_2(L) \sin[\Theta_2(L)]$$
$$\sin \mu_1 / \sin \mu_2\}, \quad i = 1, 2 \tag{28}$$

where p_2 is the impact parameter in the second sector (Fig. 7).

Equation (28) is accurate in the geometric optics approximation. In the case when refraction effect is absent in the second spherical sector, $\xi_2 = 0$, the point L_2 coincides with point L (Fig. 6), the next relationship can be used to simplify (28):

$$R_2(L) \sin[\Theta_2(L)]d_1/d_0 = R_2(L) \sin[\Theta_2(L)] \sin \mu_1 / \sin \mu_2$$
$$= R_1(L) \sin[\Theta_1(L)] \tag{29}$$

One can obtain the relationship (27) from (28) and (29). When refraction is absent in the first spherical sector, $\xi_1 = 0$, the point
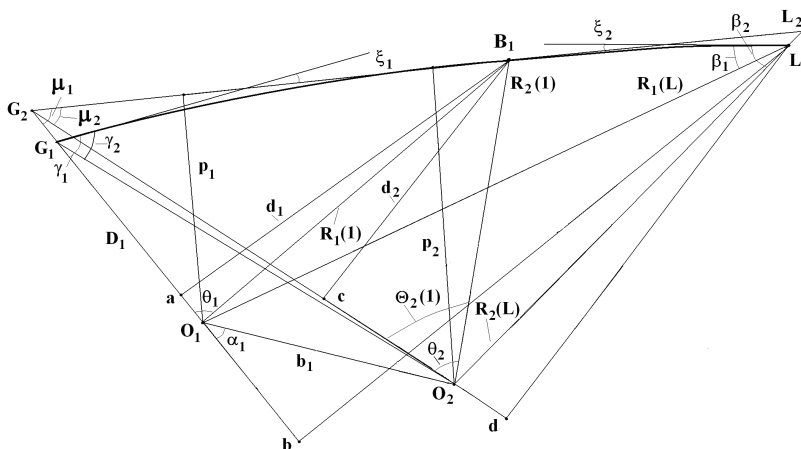
Figure 7. Propagation of electromagnetic waves through two spherical symmetric sectors.

G_1 coincides with point G, the angles μ_1, μ_2 are equal to the angles γ_1, γ_2, respectively, and one can obtain from (28):

$$X_L = R_0^2 \sin \gamma_2 / [R_2^2(L) \cos \beta_2 \, |\partial \theta_2 \, / \, \partial \gamma_2| \sin \theta_2] \qquad (30)$$

which is valid in the case of one spherical sector.

As follows from the introduced model the ionospheric contribution in the RO signals can be significant at different altitudes of the RO ray perigee in 40 km–90 km interval if the following two necessary and sufficient conditions are fulfilled: (i) the ionospheric part of the RO signals path contains a tangent point; and (ii) there is a refractivity layer with sharp gradient perpendicular to the ray $G_1B_1B_2L$ in the vicinity of the tangent point. In the simplest case, when an inclined plasma layer exists only on one part of the ray $G_1B_1B_2L$ and the influence of the neutral atmosphere is weak, the analytical model predicts the displacement of the tangent point from the ray perigee T to a plasma layer. As a result one may observe unusually strong amplitude and phase variations of the RO signals in the 40–90 km interval of the RO ray perigee height $H(T)$.

4. IDENTIFICATION OF PLASMA LAYERS

A connection between the phase excess $\Phi(p)$ (eikonal) acceleration and the refractive attenuation of electromagnetic waves $X(t)$ has been

detected and validated [27, 30, 31]:

$$1 - X(t) = ma = m\,dF_d/dt = m\,d^2\Phi(p)/dt^2;$$

$$m = q/(dp_s/dt)^2; \quad q = (R_0 - d_2)d_2/R_0 \tag{31}$$

Value m has dimension [s^2/m]. An inverse value $\frac{1}{m}$ may be considered as a module of the tangent point T centripetal acceleration oriented in the direction to point L. Formula (31) connects the refractive attenuation $X(t)$, derivative of the Doppler frequency F_d on time and the phase acceleration $a = dF_d(t)/dt = d^2\Phi(p)/dt^2$ via a relationship similar to classical dynamics equation. Variations of the refractive attenuation $1 - X(t)$ may be considered as a ratio of the eikonal acceleration and centripetal acceleration of point T. The impact parameter p_s and distances R_0 and d_2 are shown in Fig. 1. Parameters m and dp_s/dt may be evaluated from the orbital data The distance d_2 can be evaluated from the relationship [27]:

$$d_2 = 2R_0\beta[1 + 2\beta(1 - w/v) + (1 - 4\beta w/v)^{1/2}]^{-1},$$

$$\beta = mv^2/R_0, \quad m = [1 - X(t)]/a \tag{32}$$

where w and v are the velocity components of the GPS and LEO satellites, respectively, which are perpendicular to the straight line GL on the plane GOL (Fig. 1). Components w and v are positive when they oriented towards the direction to the point O and are negative in the opposite case. Analysis of the CHAMP GPS RO data indicates correctness of the relationships (31) for the atmosphere and layered structures in the ionosphere [32, 33] The relationships (31) broaden an applicability domain of the RO method. Equation (31) presents a possibility to convert the phase acceleration a and/or Doppler frequency F_d to the refractive attenuation X_p [27, 34–36]. From these derived refractive attenuation and amplitude data one can estimate the integral absorption of electromagnetic waves [27]. It is shown that there is a possibility to apply the developed technique for identification and location of sharp layered sporadic Es structures in the ionosphere [34]. This is important for study of the radio wave propagation effects in the atmospheric telecommunication links and for remote sensing of the atmosphere and ionosphere.

To consider the possibility to identify the plasma layers contribution in the RO signals we will use a CHAMP RO event 0117 (January 14, 2001, 0 h 56 m LT, 76.4 N, 172.7 W) with strong quasi-regular amplitude and phase variations. The refractive attenuation of the CHAMP RO signals at the first GPS frequency f_1 (curve 1) and phase path excesses at the GPS frequencies f_1 and f_2 (curves 2 and 3) as functions of the height of the RO ray perigee H are shown in Fig. 8 (left panel). The curves 2 and 3 have been obtained after
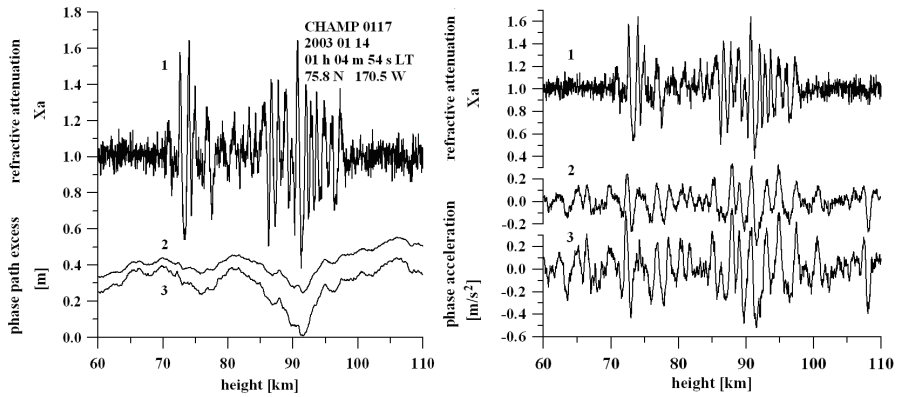
Figure 8. Refractive attenuation at the first GPS frequency f_1 (curve 1) and the phase path excesses at the frequencies f_1 and f_2 (curves 2 and 3) (left). Comparison of the refractive attenuation at the first GPS frequency f_1 (curve 1) and the phase accelerations at the frequencies f_1 and f_2 (curves 2 and 3) (right).

subtracting a regular phase trend connected with the upper ionosphere influence. The form of the refractive attenuation variations indicates the impact of the ionospheric disturbances in the 72–98 km interval of H. This disturbance consists of two patches which are responsible for the maximums in the intensity changes in the 72–78 km and 84–96 km intervals of H. In the 78–84 km interval of height H the intensity variations are notable. However they are not so strong. The phase changes at frequencies f_1 and f_2 in Fig. 8, (left panel), also indicate a two-layered structure at the altitudes 75 and 90 km. The phase accelerations at both frequencies f_1 and f_2 (curves 2 and 3 in Fig. 8, right panel) reveal the fine structures in the phase of RO signals. The phase acceleration a has been estimated numerically by double differentiation over a fixed time interval Δt. The value of Δt was equal to 0.42 s. The strongest variations of the phase acceleration are observed almost in the same altitude intervals as for the refractive attenuation. In this interval the phase acceleration and refractive attenuation variations are strongly connected and may be considered as coherent oscillations caused by layered structures. It is important that at altitudes of below 72 km and higher than 98 km the refractive attenuation variations are small and do not have any connection with changes of the phase acceleration (Fig. 8, right panel). This indicates different incoherent mechanism of the significant phase variations at the heights $H \leq 72$ km and $H \geq 98$ km. As a further identification

step, further examination is conducted to locate the indicated layers
in the ionosphere. If parameter m is estimated from the experimental
data using Equation (32), it is possible to find the new value of distance
$T'L \approx d'_2$ and to determine the displacement of the new tangent point
T' and the location of a layer relative to point T (Fig. 1):

$$d = d'_2 - (R_2^2 - p_s^2)^{1/2} \tag{33}$$

The results of parameter m, displacement d, and corrected layer height
h are given in Table 1 as a function of the altitude H of ray perigee T.
Data presented in Table 1 correspond to the CHAMP GPS RO event
No. 0117. The variations of the refractive attenuations $X_p - 1$ and
$X_a - 1$ calculated from the amplitude and phase data and the estimated
m values are shown in the second, third, and seventh columns in Table 1
as functions of the ray perigee height H in the two intervals of 97.33–
97.61 km (1); and 72.13–72.23 km (2). These intervals correspond to
a maximum in the absolute values of the refractive attenuation and
phase acceleration variations relevant to the curves 1 and 2 shown
in Fig. 8 (right panel). The displacement d and the estimated value
of the layers altitude h are presented in the forth and fifth columns
(Table 1) respectively. The displacement d changes between 140 km

Table 1. Location of ionospheric layers.

H	$X_p - 1$	$X_a - 1$	d, km	h, km	δ°	m, s^2/m
97.61	0.06429	0.07053	140.74	99.163	1.26	0.87587
97.58	0.06584	0.07291	155.00	99.461	1.38	0.88391
97.55	0.06694	0.07458	164.73	99.673	1.47	0.88940
97.52	0.06633	0.07550	198.30	100.59	1.77	0.90861
97.49	0.06610	0.07563	206.26	100.81	1.84	0.91316
97.46	0.06481	0.07478	219.46	101.22	1.96	0.92078
97.42	0.06299	0.07309	228.50	101.50	2.04	0.92599
97.39	0.06081	0.07047	226.61	101.41	2.02	0.92484
97.36	0.05814	0.06694	216.38	101.02	1.93	0.91883
97.33	0.05460	0.06265	210.95	100.81	1.88	0.91563
72.23	0.04132	0.06316	714.35	112.09	6.39	1.17436
72.19	0.04029	0.05866	626.54	102.86	5.60	1.11844
72.16	0.03934	0.05328	498.98	91.618	4.46	1.04047
72.13	0.03786	0.04721	357.26	82.105	3.19	0.95806

and 210 km in the interval (1), and 357 km–714 km in the interval (2). These values correspond to the displacement of the tangent point from the ray perigee in direction to point G. The corresponding corrections to the altitude H are about 2 km–6 km in the interval (1) and 20 km–30 km in the interval (2). This analysis suggests that the ionospheric layers are located in the entrance part of the ionosphere between point G and T (Fig. 1) at the distance d in the interval 300–500 km. The corresponding values Δh change in the 2–30 km interval. Identification of the sporadic Es layer justifies the potential applications of the Abel' transform for solving the inverse problem. The resulting electron density distribution is shown in Fig. 9. As follows from Fig. 9, the electron density variations are concentrated in the interval $0 < N(h) < 3.5 \cdot 10^{10}$ [electrons/m^3]. These magnitudes of $N(h)$ are somewhat below the usual values of $N(h)$ for sporadic E-layers. The height interval of the amplitude variations is nearly equal to the height interval of the variations in the electron density and its gradient. Two patches of the ionospheric layer are clearly seen in Fig. 9. The first patch of the layers is located on line GT at a distance 300 km from point T (curves 1 and 2 in Fig. 9). It is concentrated in the 92-104 km interval with inclination to the horizontal direction δ of about 3°. The second patch (Fig. 9, curve 3 and 4) is located on the line GT in the 94-100 km interval at the distance 500 km relative to the tangent point T (Fig. 1) with inclination of about 5°.

Between two patches the plasma density is small. The amplitude variations in the 70–96 km interval of altitude H are connected with
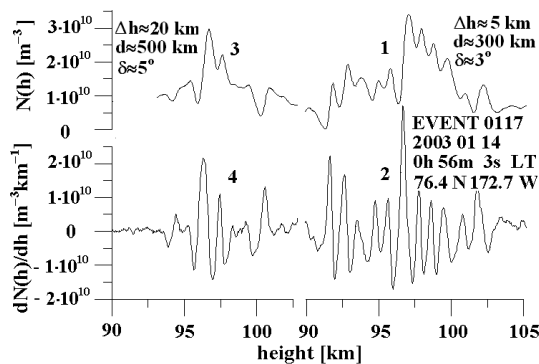

Figure 9. Vertical distribution of the electron density and its gradient in the main parts of two patches of sporadic E-layer. Curves 1 and 3 describe the electron density distribution, curve 2 and 4 relates to the vertical gradient of the electron density.

sporadic E-layer located along the line GT in the altitude interval 92–104 km at the distance 300–500 km relative to point T. The inclination of the sporadic E-layer changes along the line GT from 3° up to 5°. Therefore the introduced method appears to have a considerable potential to resolve the uncertainty in the location of the inclined layer between the part GT and LT of the ray trajectory. Additional validation of this method through analyzing the CHAMP data and comparison with ground-based ionosonde information is the task for the future work.

5. CONCLUSIONS

A new analytical model is introduced to account for local mechanism of the multiple-RO ionospheric effects which incorporates horizontal gradients in the ionosphere. The model gives analytical expressions for the phase path excess and refractive attenuation of the electromagnetic waves propagating through the disturbed ionosphere. The introduced analytical model suggests the potential for the applications of the Abel transform for estimating the electron density distribution in the inclined ionospheric plasma layers. Analysis of CHAMP RO data and the analytical model have demonstrated the importance of comparative analysis of the amplitude and phase channels of the satellite radio-holograms for classifying ionospheric influence on RO signals. Preliminary analysis reveals five types of ionospheric impacts on the CHAMP RO signals at the altitudes of RO perigee 40–90 km: (i) quiet events; (ii) isolated quasi-regular flashes (possible contribution of the inclined sporadic E-layers); (iii) events with quasi-periodical changes of the amplitude and phase (possible source — wave structures in the electron density); (iv) diffractive events with a clearly identifiable diffraction pattern in the amplitude and phase; and (v) events with noisy contribution of the ionospheric disturbances to the amplitude. The noisy and quasi-regular amplitude variations in the RO signals correspond to the earlier described C- and S-type amplitude scintillations in the trans-ionospheric satellite-to-Earth links. Analysis of the CHAMP RO data indicates a possibility of identification, location and evaluation of the electron density distribution and its gradient in the inclined ionospheric layers.

REFERENCES

1. Melbourne, W. G., E. S. Davis, C. B. Duncan, G. A. Hajj, K. R. Hardy, E. R. Kursinski, T. K. Meehan, L. E. Young, and T. P. Yunck, "The application of spaceborne GPS to atmospheric limb sounding and global change monitoring," *JPL Publication 94-18*, 147, 1994.

2. Ware, R., M. Exner, D. Feng, M. Gorbunov, K. Hardy, B. Herman, Y.-H. Kuo, T. Meehan, W. Melbourn, C. Rocken, W. Schreiner, S. Sokolovskiy, F. Solheim, X. Zou, R. Anthes, S. Businger, and K. Trenberth, "GPS soundings of the atmosphere from low earth orbit: Preliminary results," *Bull. Am. Meteor. Soc.*, Vol. 77, 19–40, 1996.

3. Kursinski, E. R., Hajj, G. A., Schofield, J. T., et al., "Observing Earth's atmosphere with radio occultation measurements using the global positioning system," *J. Geophys. Res.*, Vol. 102, 23429–23465, 1997.

4. Hajj, G. A. and L. J. Romans, "Ionospheric electron density profiles obtained with the global positioning system: Results from GPS/MET experiment," *Radio Sci.*, Vol. 33, No. 1, 175–190, 1998.

5. Steiner, A. K., G. Kirchengast, and H. P. Landreiter, "Inversion, error analysis, and validation of GPS/MET occultation data," *Ann. Geophys.*, Vol. 17, 122–138, 1999.

6. Wickert, J., C. Reigber, G. Beyerle, R. Konig, C. Marquardt, T. Schmidt, L. Grunwaldt, R. Galas, T. K. Meehan, W. G. Melbourne, and K. Hocke, "Atmosphere sounding by GPS radio occultation: First results from CHAMP," *Geophys. Res. Lett.*, Vol. 28, No. 19, 3263–3266, 2001.

7. Yakovlev, O. I., *Space Radio Science*, 306, Taylor and Francis, London, 2003.

8. Melbourne,, W. G., *Radio Occultations Using Earth Satellites: A Wave Theory Treatment*, 610, Jet Propulsion Laboratory California Institute of Technology, Monograph 6, Deep space communications and navigation series, Issued by the Deep Space

Communications and Navigation Systems Center of Excellence Jet Propulsion Laboratory California Institute of Technology, J. H. Yuen, Editor-in-Chief, 2004.

9. Jakowski, N., R. Leitinger, and M. Angling, "Radio occultation techniques for probing the ionosphere," *Annals of Geophysics, Supplement to V*, Vol. 47, No. 2/3, 1049–1066, 2004.

10. Kunitsyn, V. E. and E. D. Tereshchenko, *Ionospheric Tomography*, Springer-Verlag, Berlin, 2003.

11. Liou, Y.-A., A. G. Pavelyev, C.-Y. Huang, K. Igarashi, K. Hocke, and S. K. Yan, "Analytic method for observation of the GW using RO data," *Geophys. Res. Lett.*, Vol. 30, No. 23, ASC 1-1–1-5, 2003.

12. Igarashi, K., A. Pavelyev, K. Hocke, D. Pavelyev, and J. Wickert, "Observation of wave structures in the upper atmosphere by means of radio holographic analysis of the RO data," *Advances in Space Research*, Vol. 27, No. 6–7, 1321–1327, 2001.

13. Hocke, K., A. Pavelyev, O. Yakovlev, L. Barthes, and N. Jakowski, "RO data analysis by radio holographic method," *JASTP*, Vol. 61, 1169–1177, 1999.

14. Vorob'ev, V. V., A. S. Gurvich, V. Kan, S. V. Sokolovskiy, O. V. Fedorova, and A. V. Shmakov, "Structure of the ionosphere from the radio-occultation GPS-"Microlab-1" satellite data: Preliminary results," *Earth Observations and Remote Sensing*, Vol. 15, 609–622, 1999.

15. Steiner, A. K. and G. Kirchengast, "GW spectra from GPS/MET occultation observations," *J. Atmos. Ocean. Tech.*, Vol. 17, 495–503, 2000.

16. Igarashi, K., A. Pavelyev, K. Hocke, D. Pavelyev, I. A. Kucherjavenkov, S. Matugov, A. Zakharov, and O. Yakovlev, "Radio holographic principle for observing natural processes in the atmosphere and retrieving meteorological parameters from RO data," *Earth Planets Space*, Vol. 52, No. 14, 868–875, 2000.

17. Gorbunov, M. E., "Ionospheric correction and statistical optimization of radio occultation data," *Radio Science*, Vol. 37, No. 8, 17-1–17-9, 2002.

18. Pavelyev, A. G., Y. A. Liou, C. Y. Huang, C. Reigber, J. Wickert, K. Igarashi, and K. Hocke, "Radio holographic method for the study of the ionosphere, atmosphere and terrestrial surface using GPS occultation signals," *GPS Solutions*, Vol. 6, 101–108, 2002.

19. Liou, Y.-A., A. G. Pavelyev, C.-Y. Huang, K. Igarashi, and K. Hocke, "Simultaneous observation of the vertical gradients of refractivity in the atmosphere and electron density in the lower

ionosphere by radio occultation amplitude method," *Geophysical Research Letters*, Vol. 29, No. 21, 43-1–43-4, 2002.

20. Vorob'ev, V. V. and T. G. Krasilnikova, "Estimation of accuracy of the atmosphere refractive index recovery from Doppler shift measurements at frequencies used in the NAVSTAR system," *Izv. Russ. Acad. Sci., Physics of the Atmosphere and Ocean, Engl. Transl.*, Vol. 29, No. 10, 602–609, 1994.

21. Sokolovskiy, S. V., "Inversion of RO amplitude data," *Radio Sci.*, Vol. 35, No. 1, 97–105, 2000.

22. Sokolovskiy, S. V., W. Schreiner, C. Rocken, and D. Hunt, "Detection of high-altitude ionospheric irregularities with GPS/MET," *Geophys. Res. Lett.*, Vol. 29, No. 3, 621–625, 2002.

23. Wickert, J., A. G. Pavelyev, Y. A. Liou, et al., "Amplitude variations in GPS signals as a possible indicator of ionospheric structures," *Geophys. Res. Lett.*, Vol. 31, No. 24, ASC 1-1–1-5, 2004.

24. Liou, Y.-A., A. G. Pavelyev, C.-Y. Huang, K. Igarashi, K. Hocke, and S. K. Yan, "Analytic method for observation of the GW using RO data," *Geophys. Res. Lett.*, Vol. 30, No. 23, ASC 1-1–1-5, 2003.

25. Liou, Y. A., A. G. Pavelyev, and J. Wickert, "Observation of gravity waves from GPS/MET radio occultation data," *J. Atmos. Solar-terr. Phys.*, Vol. 67, 219–228, 2005.

26. Karasawa, Y., K. Yasukawa, and M. Yamada, "Ionospheric scintillation measurement at 1.5 GHz in mid-latitude region," *Radio Science*, Vol. 20, No. 3, 643–651, 1985.

27. Yeh, K. C. and C. H. Liu, "Radio wave scintillations in the ionosphere," *Proc. IEEE*, Vol. 70, No. 7, 324–360, 1982.

28. Liou, Y. A. and A. G. Pavelyev, "Simultaneous observations of radio wave phase and intensity variations for locating the plasma layers in the ionosphere," *Geophys Res Lett*, Vol. 33, No. 26, L23102 1–5, 2006.

29. Pavelyev, A. G., Y. A. Liou, J. Wickert, A. L. Gavrik, and C. C. Lee, "Eikonal acceleration technique for studying of the Earth and planetary atmospheres by radio occultation method," *Geophys. Res. Lett.*, Vol. 36, L21807 1–5, 2009.

30. Ahmad, B. and G. Leonard Tyler, "Systematic errors in atmospheric profiles obtained from Abelian inversion of radio occultation data: Effects of large-scale horizontal gradients," *J. Geoph. Res.*, Vol. 104, No. D4, 3971–3992, 1999.

31. Pavelyev, A. G. and A. I. Kucherjavenkov, "Refractive attenuation in the planetary atmospheres," *Radio Eng. and Electron. Phys.*,

Vol. 23, No. 10, 13–19, 1978.

32. Pavelyev, A. G., Y. A. Liou, J. Wickert, T. Schmidt, A. A. Pavelyev, and S. F. Liu, "Effects of the ionosphere and solar activity on radio occultation signals: Application to challenging minisatellite payload satellite observations," *J. Geophys. Res.*, Vol. 112, No. A06326, 1–14, 2007.

33. Liou, Y. A., A. G. Pavelyev, S.-F. Liu, A. A. Pavelyev, N. Yen, C. Y. Huang, and C.-J. Fong, "FORMOSAT-3/COSMIC GPS radio occultation mission: Preliminary results," *IEEE Transactions on Geoscience and Remote Sensing*, Vol. 45, No. 14, 3813–3826, 2007.

34. Pavelyev, A. G., J. Wickert, and Y. A. Liou, "Localization of plasma layers in the ionosphere based on observing variations in the amplitude and phase of radiowaves along the satellite-to-satellite path," *Radiophysics and Quantum Electronics*, Vol. 51, No. 1, 1–8, 2008.

35. Pavelyev, A. G., Y. A. Liou, J. Wickert, A. A. Pavelyev, T. Schmidt, K. Igarashi, and S. S. Matyugov, "Location of layered structures in the ionosphere and atmosphere by use of GPS occultation data," *Advances in Space Research*, Vol. 42, 224–228, 2008.

36. Pavelyev, A. G., Y.-A. Liou, J. Wickert, T. Schmidt, A. A. Pavelyev, and S. S. Matyugov, "Phase acceleration: A new important parameter in GPS occultation technology," *GPS Solutions*, Vol. 14, No. 1, 3–14, 2010.